nature communications

Article

https://doi.org/10.1038/s41467-026-74873-5

Volcanic eruptions caused weakening AMOC during the preindustrial past millennium

Received: 11 March 2025

Accepted: 15 June 2026

Published online: 27 June 2026

Check for updates

Kefan Chen[1,2], Zhengyu Liu[3], Liang Ning[1,2], Jian Liu[1,4,5], Lili Lei[6,7], Michael E. Mann[8], Mi Yan[1], Weiyi Sun[1], Haohao Sun[7], Wenqing Hu[1], Peng Gu[9], Yuntao Bao[10], Yanmin Qin[11], Fangmiao Xing[1], Lingwei Li[12], Jinbo Du[13] & Qin Wen[1]

The Atlantic Meridional Overturning Circulation (AMOC) is a key component of our climate system. However, the evolution history and the forcing mechanism of AMOC in the last millennial has remained uncertain. Here, combining available paleo AMOC-sensitive indicators with multiple climate models and paleo Data Assimilation, we show, for the first time, that the AMOC transport exhibits a slow declining trend into the Little Ice Age, with a reduction of about $-0.7 \pm 0.4Sv.$ (~4%) from AD 850-1850. This weakening is mainly caused by explosive volcanic eruptions. After a rapid strengthening in the initial decade following a volcanic eruption, the AMOC tends to show a slow weakening of centennial timescale, driven by stored cooling in the deep Atlantic and its feedback on North Atlantic climate.

The Atlantic Meridional Overturning Circulation (AMOC) strongly impacts the global climate from decadal to millennial time scales through the modulation of the poleward heat transport[1,2]. During the past glacial-interglacial cycles, rapid climate changes have occurred along with abrupt changes of climate and meltwater flux in the North Atlantic region, possibly associated with AMOC instability[3,4]. In the modern instrumental era, there appears to suggest a slowdown of the AMOC[5–7], likely in response to the increased surface heat flux associated with anthropogenic global warming[8], leading some to hypothesize that the AMOC may collapse in the near future[9]. In the past millennium before the Industrial Revolution, studies using paleo "AMOC-sensitive indicators" infer a slow decline of AMOC from the relatively warm period broadly termed the Medieval Climate Anomaly (MCA) (AD 850–1250) to the relatively cold period broadly termed the Little Ice Age (LIA) (AD 1250–1850)[10–18]. These diverse sets of purported AMOC-sensitive indicators have left fundamental questions wide open. Dynamically, are the weakening signals among these AMOC-sensitive indicators consistent? Quantitatively, how much is the weakening of the AMOC transport? Physically, what is the cause of the weakening trend? Some past studies have emphasized the potential role of internal variability[19], while others have instead proposed external forcing mechanisms[20–22]. Past studies indicate an important role for

[1]State Key Laboratory of Climate System Prediction and Risk Management; Key Laboratory for Virtual Geographic Environment of Ministry of Education; State Key Laboratory Cultivation Base of Geographical Environment Evolution and Regional Response of Jiangsu Province; Jiangsu Center for Collaborative Innovation in Geographical Information Resource Development and Application; School of Geography, Nanjing Normal University, Nanjing, China. [2]College of Geography and Remote Sensing Science, Xinjiang Key Laboratory of Oasis Ecology, Xinjiang University, Urumqi, China. [3]Department of Geography, The Ohio State University, Columbus, OH, USA. [4]Open Studio for the Simulation of Ocean-Climate-Isotope, Qingdao National Laboratory for Marine Science and Technology, Qingdao, China. [5]Jiangsu Provincial Key Laboratory for Numerical Simulation of Large Scale Complex Systems, School of Mathematical Science, Nanjing Normal University, Nanjing, China. [6]Key Laboratory of Mesoscale Severe Weather, Ministry of Education, and School of Atmospheric Sciences, Nanjing University, Nanjing, China. [7]Frontiers Science Center for Critical Earth Material Cycling, Nanjing University, Nanjing, China. [8]Department of Earth and Environmental Science, Annenberg School for Communication, University of Pennsylvania, Philadelphia, PA, USA. [9]School of Mathematics, The University of Edinburgh, Edinburgh, UK. [10]Nanjing-Helsinki Institute in Atmospheric and Earth System Sciences, Nanjing University, Suzhou, China. [11]Guangxi Laboratory on the Study of Coral Reefs in the South China Sea, Coral Reef Research Centre of China, School of Marine Sciences, Guangxi University, Nanning, China. [12]Department for Atmospheric and Oceanic Sciences and Institute of Arctic and Alpine Research, University of Colorado Boulder, Boulder, CO, USA. [13]Department of Atmospheric and Oceanic Sciences, Peking University, Beijing, China. e-mail: liu.7022@osu.edu; ningliangnnu@njnu.edu.cn

volcanic forcing in driving multidecadal periods of cooling in the North Atlantic during the LIA[23,24]. Such cooling can lead to AMOC weakening due to sea ice expansion and associated positive air-sea feedbacks[25]. This mechanism, however, has been challenged by modeling studies that instead show a strengthening of the AMOC following episodes of volcanic activity due to large-scale cooling[26–29] and associated change in atmospheric and oceanic circulation[30–32]. Some model simulations also suggest a slight weakening for a decade after the initial intensificiation[25,31]. However, it remains unclear how the short-term radiative forcing from an explosive volcanic eruption can induce centennial-scale AMOC weakening.

Here, we seek to answer these questions by comprehensively examining paleo AMOC-sensitive indicators and the AMOC response to volcanic eruptions over the past millennium in multiple state-of-the-art earth system models, including, in particular, the water isotope-enabled NCAR CESM ("Methods"). We show that the various AMOC-sensitive indicators are dynamically consistent and collectively imply a declining AMOC trend during the past millennium, i.e., over the course of the MCA/LIA transition. Furthermore, using paleo data assimilation (PDA) with these AMOC-sensitive indicators, we yield the first estimation of the reduction of AMOC transport. Finally, we propose a mechanism for explaining the centennial-scale response to volcanic eruption, which involves a combination of fast and slow components of the AMOC related to the response of North Atlantic Deep Water (NADW), the atmospheric hydrological cycle, and freshwater oceanic input.

Results

Observed weakening of AMOC in the LIA

We first show that paleo AMOC-sensitive indicators of the past millennium display overall a clear weakening trend in the AMOC during the transition from the MCA to LIA. Because direct observations of AMOC are unavailable until 2004, AMOC change before 2004 must be indirectly inferred from oceanic variables related to the AMOC, or "AMOC-sensitive indicators."[6,7] In the last millennium, most of which occurs before the instrumental period, these oceanic variables can only be reconstructed from proxy records. Thus, AMOC change in the last millennium must be indirectly inferred from these proxy-based AMOC-sensitive indicators. Figure 1a–e (color lines) show five paleo AMOC-sensitive indicators ("Methods"): three represented by calcite $\delta^{18}O$ related to the Florida Current Transport[12], the upper ocean thermal stratification[10,20] and the distribution of slope water at Laurentian Channel[16], and two represented by temperature proxies associated with the dipole in North Atlantic subsurface temperature[14] and the North Atlantic "warming hole."[6] We note that these proxy-based indicators have low temporal resolution and large chronology uncertainties; physically, different indicators also have different response time scales from the true AMOC transport. Thus, they can't be used to study the details of the variability and timing of AMOC changes relative to volcanic events. However, they could provide robust information on the overall trend of the AMOC from MCA to LIA. This will be our focus here. These AMOC-sensitive indicators show a declining trend from the MCA towards the LIA. Despite some differences in the precise timing of AMOC reduction across the reconstructed AMOC proxies—which could be attributed to chronology uncertainties and differing response timescales[14]—these proxy records consistently indicate a significant weakening in the LIA relative to the MCA, with notable decreases occurring around 1300 CE (Fig. 1a), 1450 CE (Fig. 1b, d), 1600 CE (Fig. 1c) and 1250 CE (Fig. 1e) across the five proxies, and around 1250 CE for their composition (Fig. 1f). Given the chronology uncertainty and low temporal resolution of the proxies, these periods can be considered broadly coinciding with marked increases in explosive volcanic radiative forcing in the 13th, 15th, and 17th centuries[33–35] (Fig. 1a–g). These observations seem to indicate a possible relation between the AMOC decline trend and the pervasive explosive volcanic eruptions during the LIA, a key hypothesis that will be studied in detail later.

The fidelity and dynamic consistency of this diverse set of AMOC-sensitive indicators in representing the AMOC decline are further validated in the state-of-the-art Earth System Model-iCESM. We examine 16 transient simulations of the last millennium in CESM (LME), including three members with stable water isotopes in iCESM (iLME) ("Methods"). These simulations are used as they are the only published past millennium simulations enabled with oxygen isotopes and having multiple ensemble members under full and single external forcings. Furthermore, CESM is a state-of-the-art Earth system model that has been used and tested worldwide, with reasonably realistic AMOC representation[36,37]. Treating each simulation as a single real-world realization, we reconstruct the two temperature AMOC-sensitive indicators from the model variables in all the 16 simulations, and the three $\delta^{18}O$ indicators in the 3 iLME simulations ("Methods" and Fig. S1a). The correlations between the model AMOC-sensitive indicators and the AMOC transport index show that approximately 3/4 of the cases are statistically significant, with generally high correlation coefficients across the simulations (Fig. S2a). This suggests that most of the AMOC-sensitive indicators are dynamically consistent within the CESM model physics, representing different aspects of the AMOC. As an example, Fig. 1h–l shows the time evolution of the five model indicators (color lines) in comparison with the model AMOC (black dash line) in one simulation (case iLME1, see "Methods" for why iLME1 is selected, Fig. S2a marked with red stars). It is seen that, like the true AMOC, almost all the synthetic AMOC-sensitive indicators significantly decrease in the LIA relative to the MCA ($p < 0.1$), particularly with a transition from positive to negative phases (i.e., from above to below long-term mean) after strong volcanic eruptions in 1176–1284 (Fig. 1n). This confirms that the declining AMOC in the real world can be well simulated in the model and is therefore dynamically consistent. This overall declining trend can be seen more clearly after a 200-year low-pass filter or a reduction of temporal resolution using a 150-year window (Fig. S3a–g), both of which retain the declining trend of AMOC by smoothing out decadal variability signals. This low-pass AMOC is of a more compatible resolution with those of the real-world proxy records. This further suggests that these coarse resolution proxies can represent the overall declining trend of the AMOC, but not the multidecadal variabilities.

Our simulations further show that AMOC variation can be represented best by a composite AMOC index that is the simple average of the five AMOC-sensitive indicators, each normalized by its standard deviation, due presumably to the suppression of noise by average (Fig. 1m). Indeed, this composite AMOC index has a higher correlation with AMOC and is therefore superior than any single AMOC-sensitive indicator across almost all the simulations (Fig. S2b yellow bars vs. white bars). This motivates us to also construct the composite AMOC index in observations by averaging the five paleo AMOC-sensitive indicators after normalization and temporal interpolation (Fig. 1f). The slow weakening trend of AMOC is more clearly shown in the composite index in observations and the model (Fig. 1f, m). Beyond the trend, however, there is little sign of coherent variability in the composite index in the observation. This is an additional indication of the chronology uncertainty in the proxy records, supporting our assertion that these proxies likely only provide useful information on the overall trend of the pre-industrial past millennium.

The covariance between these AMOC-sensitive indicators and the AMOC in models also allows us to reconstruct the AMOC transport evolution by combining the observational AMOC-sensitive indicators with the model simulations using an off-line PDA approach ("Methods"). This PDA method can quantify the decline transport of the AMOC (in Sv), beyond the AMOC-sensitive indicators that only show a qualitative trend. In addition, the PDA effectively combines all AMOC-sensitive indicators together in a dynamically consistent way,

https://doi.org/10.1038/s41467-026-74873-5

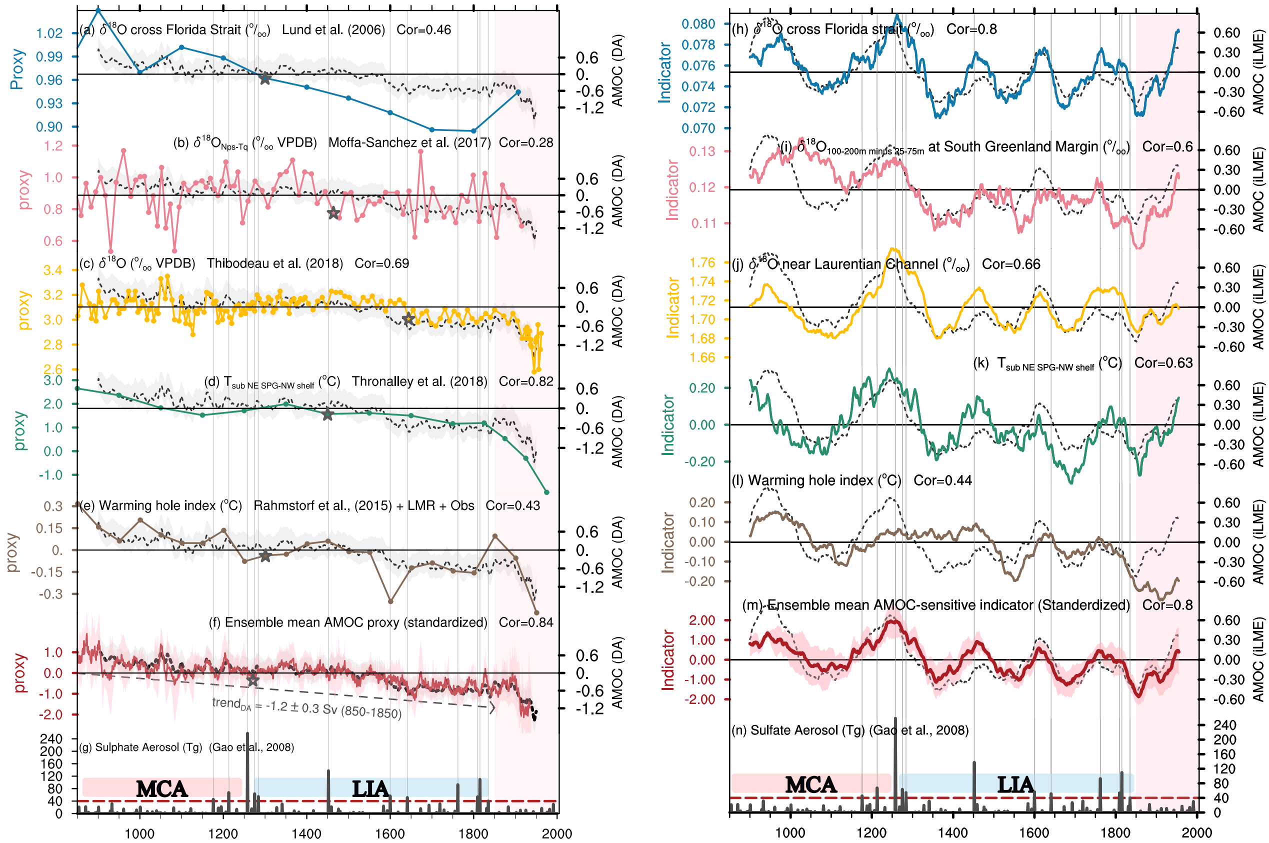

Fig. 1 | AMOC-sensitive indicators reconstructed by proxies and model simulations. Colored solid lines are the reconstructed Atlantic Meridional Overturning Circulation (AMOC) proxies ("Methods"), including **a** difference of benthic $\delta^{18}O$ (‰) cross the Florida Strait[12]; **b** difference of $\delta^{18}O$ (‰) from two kinds of planktonic foraminifera living at different depths at the South Greenland Margin[10,20]; **c** $\delta^{18}O$ (‰) in benthic foraminifera at the Laurentian Channel[16]; **d** difference of subsurface ocean temperature between north-east Subpolar Gyre (SPG) and north-west Atlantic shelf[14]; **e** warming hole index calculated by the reconstructed proxies[6,65] and observational data[66–68]. **f** Average of the standardized AMOC proxies in (**a**–**e**), which are interpolated into annual temporal resolution and applied with a 51-year running mean. The pink spread indicates the ±1 standard deviation. The black dashed lines in (**a**–**f**) are the assimilated AMOC proxies (unit: Sv) generated by a paleo-data assimilation (PDA) approach ("Methods"). The gray shading denotes the central 90% region from 5 to 95%. The trend of the PDA AMOC proxy is −1.2 ± 0.3 Sv ("Methods"). The correlation coefficients between reconstructed and assimilated AMOC proxies are marked on the top of each figure. Gray asterisks mark the onset of significant AMOC decrease relative to the Medieval Climate Anomaly (MCA) ($p < 0.1$) in each panel. **h**–**l** Colored solid lines are the best AMOC-sensitive indicators (Y-axis on the left side) reproduced by one of the iLME model simulations (iLME1, details in "Methods" and Fig. S2), using the same reconstructed methods as the AMOC-sensitive indicators in (**a**–**e**), respectively ("Methods"): **h** contrast of $\delta^{18}O_c$ (‰) cross the Florida Strait, **i** South Greenland Margin subsurface-surface $\delta^{18}O_c$ difference (‰), **j** Laurentian Channel $\delta^{18}O_c$ (‰), **k** upper ocean temperature contrast between north-east SPG and north-west Atlantic shelf, and **l** warming hole index. **m** Composite of the standardized reproduced AMOC-sensitive indicators in (**h**–**l**). The pink spread indicates ±1 standard deviation. The black dashed lines in (**h**–**m**) are the true AMOC (Y-axis on the right side) output from the iLME model simulation in case 1 (Fig. S2). The simulated AMOC and AMOC-sensitive indicators are applied with a 101-year running mean, and the correlation coefficients ($p < 0.1$) between them are shown on the top of each figure. **g**, **n** Are the global volcanic aerosol injection reconstructed by Gao et al.[33]. The red dashed line indicates volcanic magnitude larger than 40 Tg. Gray vertical shadings highlight the volcanic eruptions with magnitudes larger than 40 Tg.

suggesting the dynamic consistency among the indicators. The assimilated AMOC transport index (Fig. 1a–f, black dashed line) is highly correlated with each paleo AMOC-sensitive indicator (Fig. 1a–e, colored solid line), and particularly the composite index (Fig. 1f). The PDA AMOC transport in CESM quantifies an overall declining AMOC transport trend in AD 850–1850 as -1.2 ± 0.3Sv. Given the observed AMOC transport of about 17 Sv[38], this represents a reduction of about 7%. This reduction is about twice that in the simulation of iLME1 (-0.67 Sv), because the magnitude of reduction in the observed AMOC-sensitive indicators are larger than the simulation.

This PDA AMOC estimation is based on the CESM alone and therefore may be subject to substantial model uncertainty. As a more comprehensive estimation, we make use of 4 additional last millennium simulations in 4 PMIP models that are available ("Methods"). The AMOC transport can be assimilated similarly as for the iCESM in each PMIP model, except that only two temperature AMOC-sensitive indicators are assimilated, because of the lack of water isotopes in these PMIP models ("Methods"). Each of the assimilated AMOC index in PMIP models shows a significant declining trend, although the original simulations in PMIP models only show AMOC weakening after major volcanic eruptions (to be discussed later) without a clear long-term trend (Fig. S4b–f). Combining the 5 AMOC estimations in 5 models leads to our final multi-model AMOC estimation, which shows a declining trend of $-0.7 \pm 0.4Sv.$ in AD 850–1850 (about 4% of the total transport) ("Methods").

The CESM model simulation further shows that the AMOC and AMOC-sensitive indicators tend to first peak in the initial decade and then decline to a minimum in about a hundred years after strong volcanic eruptions in the 13th, 15th, 17th, and 19th centuries (gray shadings in Fig. 1h–n). This asymmetric strengthening/declining behavior is seen more clearly in the time series with 11-year running mean before centennial low-pass filter in both CESM-LME archieve (Fig. S3h–n) and multi-model simulations from PMIP (Fig. S4b–f). This AMOC response phase relation with volcanic eruption, and the accompanying declining trend in LIA, leads us to hypothesize that the slow decline trend is caused predominantly by volcanic eruptions. This hypothesis is consistent with the even more clear signals in the cross-member ensemble means of AMOC and AMOC-sensitive indicators in CESM, which reflect more the forced response to external forcing (Fig. S3o–u).

Volcanic impacts on AMOC during the past millennium

We now further study the detailed AMOC response processes during the LIA. We first confirm the role of volcanic eruption on slow AMOC weakening by noting the similar AMOC evolution in the CESM-LME archives between the ensemble of simulations forced by all forcing (AF EXP) and those by the volcano-only forcing (VOLC EXP) ("Methods"). In both sets, in each simulation, strong volcanic eruptions in LIA cause a sharp decrease of surface air temperature (SAT) in the mid-13th, mid-15th, and 17th–19th centuries that nevertheless quickly recovers following the eruption (Fig. 2a–c). Unlike the short response of SAT changes, four of major centennial AMOC events occur, apparently corresponding to four periods of enhanced volcanic activities (>40 Tg) in AD 1176–1284, 1452, 1600–1641, and 1762–1835 (Fig. 2a–c). Each AMOC event is featured by a sharp intensification phase followed by a slow weakening phase. The detailed features of the AMOC response to each volcanic event, unfortunately, can't be tested in the available paleo AMOC-sensitive indicators, because of their coarse resolution and large uncertainty in chronology. Furthermore, on the longer millennial time scale, AMOC exhibits a slow decline trend from the MCA to the LIA in both forcing scenarios. Since the VOLC ensemble is forced by volcanic eruption only, the strong similarity of AMOC evolution between the AF EXP and VOLC EXP suggests that the four centennial AMOC events and the slow decline trend are caused by volcanic eruptions. Note that the slow decline of the fourth AMOC events in response to the strong volcanic events of 1762–1835 continues to 2005 in the VOLC EXP, but not in the AF EXP. This is because, in AF EXP, AMOC is strengthened by increased anthropogenic aerosols in the last half century, which has overwhelmed the AMOC weakening in response to rising atmospheric CO_2 concentrations[39].

One notable feature of the AMOC centennial events is a strong asymmetry between the fast intensification and slow weakening, or between the short strong (positive) phase and long weak (negative) phase (relative to the long-term mean), as shown more clearly in the evolution before the centennial low-pass (Fig. 2a, b). Figure 2d compares the lengths between the positive and negative phases for the four centennial AMOC events in both the AF EXP and VOLC EXP ensembles. The strong/positive phase lasts on average less than 60 years for most events, while the weak/negative phase mostly lasts longer than 100 years. The longest negative phase of AMOC occurs after volcanic eruptions of 1762–1835 and lasts more than ~150 years when forced by the volcanic forcing only (VOLC EXP). This long negative phase, however, is only terminated by the intensification after about 1900 when all forcings are applied, mostly by the anthropogenic aerosol (Fig. 2a). Therefore, this volcano-induced AMOC weakening event would have persisted till the present if not interrupted by other external forcings. The impact of volcano forcing on the centennial AMOC variability can also be seen in that both the positive and negative phases are substantially longer than those in the control simulation without external forcing, which are about 20 years (Fig. 2d). This asymmetric response feature also appears robust in PMIP/CMIP multi-model simulations (Fig. S4). The four PMIP simulations, driven by different reconstructed volcanic forcings[33–35] ("Methods"), consistently show a decadal-scale AMOC strengthening followed by prolonged weakening after major volcanic eruptions in the past millennium (Fig. S4b–e). Despite the differences in the timing and magnitude of the volcanic aerosols used, the AMOC response remains robust across the four models, particularly in the composited result, with natural variability being reduced (Fig. S4f). The asymmetric AMOC response, characterized by an initial short-term strengthening followed by a long-term weakening, is more clearly revealed by the superposed epoch analysis of major volcanic eruptions in both multi-model and CESM-LME simulations (Fig. S4j–o). These analyses highlight the volcanic eruptions as the key external forcing agent that generates the centennial AMOC events and, ultimately, the millennial weakening trend in LIA.

AMOC response to a single volcanic eruption

Given that the CESM-LME simulations include mixed volcanic forcing, the impact of individual eruptions is difficult to isolate[40]. We therefore examine the idealized AMOC response to a single large volcanic eruption to illustrate the underlying mechanism. We perform a 10-member ensemble of simulations, each of 360 years, forced only by the sulfate aerosol of Mt. Samalas (AD 1258, 257.91 Tg, Fig. 3a1) injected into the stratosphere at a strong AMOC phase (Samalas EXP, "Methods"). The ensemble mean AMOC response shows a rapid intensification initially, peaking at year 7, and a subsequent slow weakening of hundreds of years. As such, the AMOC stays in the strong/positive phase for ~60 years before it declines to a long weak/negative phase of 300 years (Fig. 3a). The averaged anomalies (relative to the long climatology of CTRL EXP) in year 60–360 are significantly negative (-0.31 ± 0.16 Sv), although the variability in each year has large spread due to internal variability. Note that, although the duration of the positive phase in Samalas EXP is comparable to those in CESM-LME, the negative phase is much longer than those in CESM-LME (Fig. 2d, bold boxes). This longer negative phase in Samalas EXP is caused partly by the absence of volcanic eruptions after the single eruption. In comparison, in CESM-LME, volcanic eruptions occur frequently, such that a weak/negative phase of AMOC is often terminated by the intensification forced by the closely followed eruptions years to decades later. Two additional sets of sensitivity experiments, each with three ensemble members, are also conducted by imposing the Samalas volcanic forcing, one at a neutral state and one at a weak AMOC state in CTRL ("Methods"). As shown in Fig. S5, the response of AMOC exhibits similar asymmetric patterns of initial decadal intensification followed by a centennial weakening following volcanic eruptions, regardless of the initial states. This indicates that the AMOC response is insensitive to the initial state of the AMOC, and that the centennial-scale AMOC weakening is primarily a consequence of volcanic forcing rather than a long natural variability mode. Overall, these volcanic experiments show that, after the initial decades of intensification, a short volcanic forcing can induce a slow centennial weakening that is much longer than the decadal climate impact suggested by previous work[26,31].

Mechanisms of volcano-induced long-term AMOC weakening

The response of AMOC to a single volcanic eruption, such as the Samalas eruption, can be understood in three stages: the initial intensification stage, the early decline stage, and, eventually, the long weak stage. Here, the mechanism for the first stage of rapid intensification will be discussed only briefly, because it is consistent with extensive previous work[26,30,32]. We will focus on the mechanisms of the last two stages, especially the last stage of slow weakening. The key question is whether a short volcanic eruption can cause a slow AMOC weakening of hundreds of years?

Immediately after the volcanic eruption, the AMOC starts to increase in year 2 with the peak in year 7, as seen in the initial annual evolution (Fig. 3a1). This initial intensification is forced primarily by the sharp intensification response of the atmospheric circulation of the North Atlantic Oscillation (NAO) (Fig. S6a). Such a response has been suggested in previous studies to be associated with enhanced meridional temperature and pressure gradient in the stratosphere caused by volcanic aerosols, which in turn strengthens the stratospheric polar vortex and drives its propagation downward through stationary waves[41–44]. The intensified NAO strengthens the surface westerlies

https://doi.org/10.1038/s41467-026-74873-5

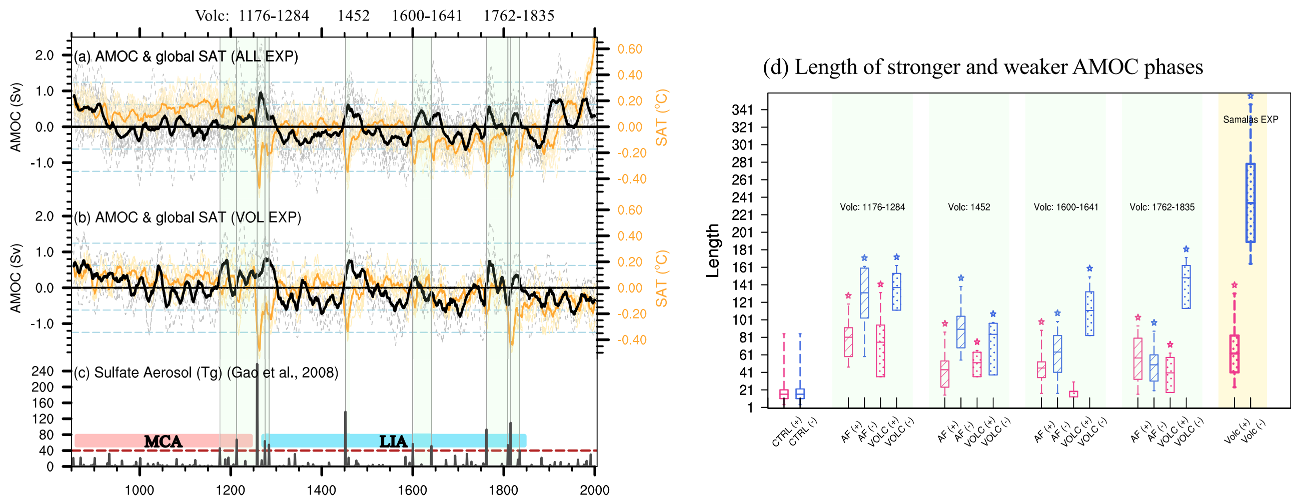

Fig. 2 | Features of AMOC and global surface air temperature (SAT) during the past millennium. a, **b** Ensemble mean AMOC anomalies (unit: Sv, black solid lines, Y-axis on the left side) and global SAT (unit: °C, orange solid lines, Y-axis on the right side) spanning from AD 850 to 2005 in the 13 ALL EXP and 5 VOLC EXP in CESM-LME[62]. Black and orange dashed lines are AMOC and SAT in each ensemble member, respectively. The dashed horizontal lines are ±1 and ±2 standard deviations of the long-term climatology of AMOC. **c** Sulfate volcanic aerosol reconstructed by Gao et al.[33]. The red dashed horizontal line indicates the magnitude of volcanic eruption at 40 Tg. The gray shadings highlight volcanic eruptions larger than 40 Tg. The green shadings highlight the 4 periods of strong (>40 Tg) volcanic activities during the Little Ice Age (LIA), including AD 1176–1284, 1452, 1600–1641, and 1762–1835. **d** Box-and-whisker diagram of the persistent time of stronger (magenta) and weaker (blue) AMOC phases (relative to long time climatology) in CESM-LME simulations and Samalas-only EXP. The 1st column shows the persistent time of stronger and weaker AMOC phases in the CESM-LME CTRL experiment. The 2nd–5th columns (shaded by green) are the length of the initial increased and subsequent decreased AMOC anomalies triggered by the 4 frequent volcanic eruptions (shaded by green in **c**) in the ALL (filled by lines) and VOLC (filled by dots) EXP from CESM-LME. The last column (shaded in yellow) shows the persist time of the initial increased and following decreased AMOC phases after one single volcanic eruption in the Samalas EXP. The line in the middle of the box is the averaged length, the upper and lower lines are the third and first quartiles, and the upper and lower whiskers are the maximum and minimum length. The star indicates that the length of the volcano-induced AMOC anomaly is significantly longer than the Ctrl experiment ($p < 0.05$).

(Fig. S6a), and, in turn, evaporation (Figs. 3c1 and S6b, c), leading to a positive salinity and then density anomaly in the high latitude North Atlantic with the peak in year 4 (Fig. 3b1). This density anomaly then intensifies the AMOC with the peak delayed 3 years later[30]. In comparison, the volcanic-induced cooling and sea ice melting water contribute little to the density anomaly (Figs. 3b1, e1, and S6c).

After the peak at year 7, the AMOC starts to decline, caused by the expansion of Arctic sea ice and the export of sea ice melting water at the edge of the sea ice in the early decades (Fig. 3e2)[45,46]. A few years after the eruption, the NAO anomaly diminishes, so is the anomalous evaporation and the resulting freshwater flux (Fig. 3c2). Instead, Arctic sea ice expands to its maximum around year 10 (Fig. 3e2) over the Labrador Sea (LS), Irminger Sea, and GIN Sea (Fig. S7f). The freshwater associated with the sea ice melting each summer is then exported along the sea-ice edge to the subpolar North Atlantic (Figs. 3e2 and S7d, e), freshening the surface water over the North Atlantic deep convection regions, suppressing deep convection, the AMOC and, in turn, the related poleward heat transport (Figs. 3b2, c2, and S7a–c). This is consistent with previous findings of sea ice expansion and Arctic freshwater export at the onset of LIA, as observed in reconstructed records[21,45,46]. This sea ice melting effect lasts for decades, bringing the AMOC back to its initial strength in about 60 years.

The AMOC continues to decline gradually after year 60 and then remains in the weak/negative phase for almost three hundred years (Fig. 3a1). This long weakening of AMOC is caused by the reduced evaporation and the resulting surface freshening over the deep convection region, and ultimately by the subsurface cooling of the NADW.

In this long weak stage, the surface density is reduced over the deep convection region around the Irminger Sea and Iceland-Faroe-Scotland Ridge, primarily due to decreasing salinity, which overwhelms the effect of SST cooling that would otherwise increase density (Figs. 3b2 and 4a–c). The long-term surface freshening is caused by the centennial-scale decrease of evaporation over the same regions (Fig. 3c2 and 4d, e).

The long-term decease of evaporation is caused by a sustained cooling over the subpolar North Atlantic (Fig. 3b2), which reduces the saturation specific humidity (q_s) and, in turn, the difference between q_s and air specific humidity (q_a) (Figs. 3d2 and 4c). Since the 850 hPa wind speed anomalies are insignificant and inconsistent with evaporation changes (Fig. 3d2), they cannot be the main contributor to the long-term evaporation decline. Our results also indicate that the sustained surface cooling is primarily driven by oceanic processes, specifically subsurface cooling, rather than atmospheric processes through radiative forcing anomalies. This can be seen in the response of the net surface heat flux and its decomposition into sensible, latent, shortwave, and long-wave components (positive downward). The anomalous net surface heat flux remains positive during this period, mainly due to the decreased latent heat loss associated with reduced evaporation (Fig. S8). This heat flux anomaly alone would have warmed the SST, which is opposite to the observed surface cooling, indicate that long-term cooling is maintained by oceanic processes instead of atmospheric ones. This point to infer the forcing mechanism of SST from surface heat flux has been studied extensively in recent studies[47–50]. Figure 5 shows that the volcanic eruption causes cooling penetrating into the subsurface North Atlantic high latitude to 2000 m in the initial decade through the deep convection and mixing (year 0–9, Fig. S9a). In the following decades, the cooling is strengthened in the subsurface ocean for hundreds of years, due to large ocean heat capacity[51–53], even if the surface cooling is reduced after the termination of the direct volcanic forcing. This strengthening subsurface cooling is caused partly by the southward export of the NADW, and partly by the ventilation of Antarctica Intermediate Water from the Southern Ocean via the Deacon Cell (10–60 years, Fig. S9b). This subsurface cooling remains substantial for hundreds of years (Figs. 5 and S9c) and is mixed upward in the high latitude North

https://doi.org/10.1038/s41467-026-74873-5

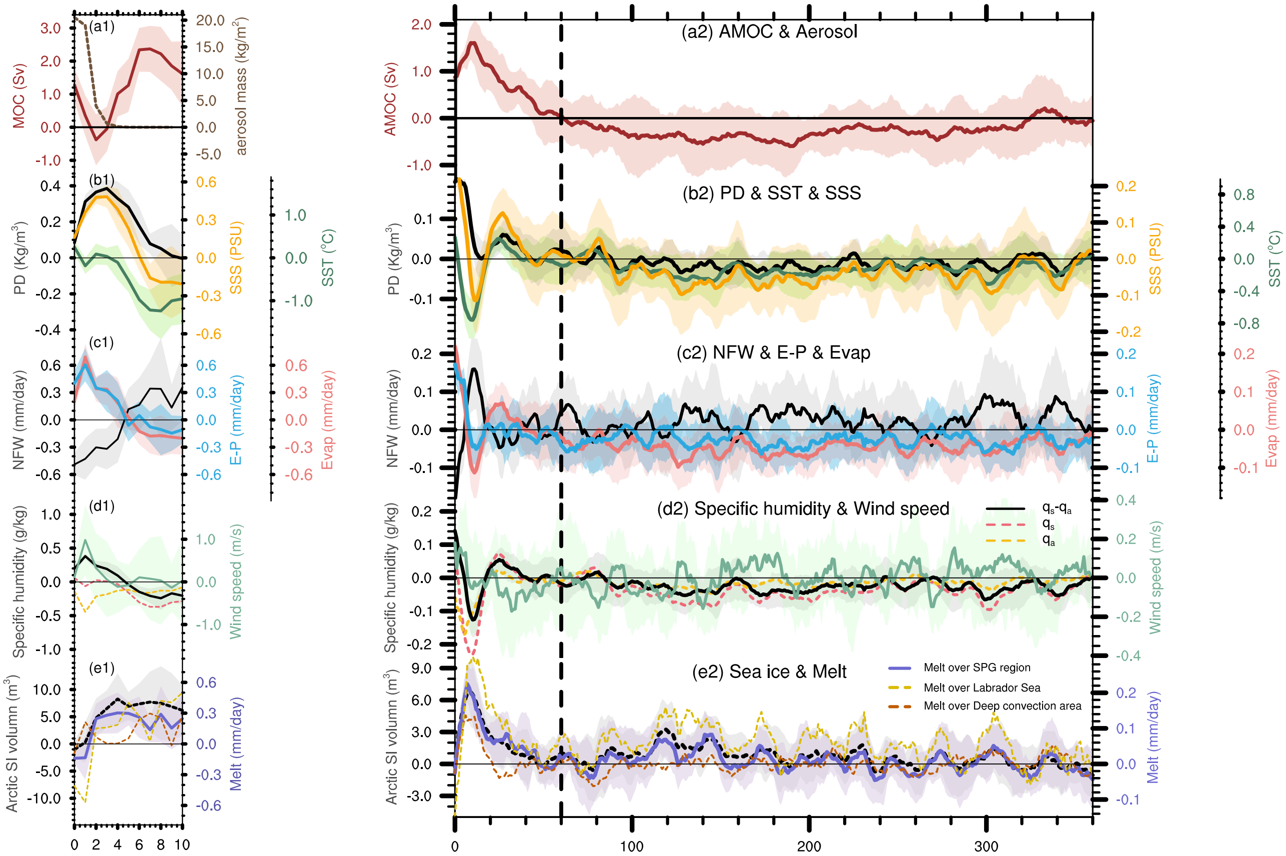

Fig. 3 | Evolution of AMOC and related variables in the Samalas-only sensitivity experiments. a Ensemble mean anomalies of AMOC (unit: Sv, red line, Y-axis on the left side) after volcanic eruptions in the 10 cases of Samalas-only EXP. Time series without running mean in the first 10 years of volcanic eruption is shown in (a1), and time series applied with 11-year running mean is shown in (a2). The brown dashed line in (a1) indicates the reconstructed global aerosol mass[33] released by MT. Samalas (unit: kg/m^2, Y-axis on the right side). **b** Ensemble mean anomalies of neutral potential density (PD, black line, unit: kg/m^3), sea surface salinity (SSS, yellow line, unit: PSU), and sea surface temperature (SST, green line, unit: °C) averaged over the deep convection region (Fig. S1b), without (b1) and with (b2) 11-year running mean. **c** Is similar to (**b**), but for net freshwater flux (NFW, black line, unit: mm/day), evaporation minus precipitation (E-P, blue line, unit: mm/day), and evaporation (pink line, unit: mm/day). **d** Is similar to (**b**), but for the saturated specific humidity (q_s, red dashed line, unit: g/kg), air specific humidity (q_a, yellow dashed line, unit: g/kg), difference between q_s and q_a (black solid line, unit: g/kg), and 850 hPa wind speed (green solid line, unit: m/s). **e** Ensemble mean anomalies of the Arctic Sea ice volume (SI, black solid line, unit: m^3), and the anomalous sea ice melt (unit: mm/day) distributing at the SPG region (purple solid line), Labrador Sea (yellow dashed line) and deep convection region (brown dashed line, Fig. S1b), respectively, without (e1) and with (e2) 11 year running mean. The shadings in (**a**–**e**) indicate the ±1 standard deviation of each variable. The anomalies are relative to the long-term climatology of CTRL EXP. Note that the averaged anomalies of AMOC, PD, SST, SSS, NFW, E-P, Evap, and q_s-q_a in the years 60–360 are significant relative to zero ($p < 0.05$). The vertical dashed line in (a2–e2) marks the transition time of AMOC from positive to negative phase. The eruption of the volcano starts in year-0.

Atlantic, leading to the long-term surface cooling in the North Atlantic. The subsurface cooling doesn't recover until 300 years after the volcanic eruption (Fig. S9d). Thus, ultimately, the slow weakening of AMOC is caused by the cooling stored in the subsurface ocean, consistent with proxy reconstructions that show significant cooling in the surface[54–56], subsurface[57], and intermediate North Atlantic after the 13th century[58]. This slow weakening of AMOC may be further reinforced by the Arctic sea ice expansion and oceanic heat transport of the North Atlantic Subpolar Gyre (SPG) (Supplementary Text, Fig. S10)[59,60]. The Samalas eruption represents an exceptionally strong forcing compared to other eruptions over the last millennium. The mechanisms identified here and their insensitivity to the initial AMOC state may therefore differ from those associated with more moderate eruptions[40], an aspect required further investigation. On the other hand, solar variability may[61] or may not[31] contribute substantially to the AMOC changes, and its role also requires further investigation.

Discussions

Our study shows that the diverse set of available paleo AMOC-sensitive indicators for the past millennium are dynamically consistent. These AMOC-sensitive indicators, when assimilated into multi-model simulations, give an estimation of weakening AMOC transport of $0.7 \pm 0.4 Sv$. (about 4% of the total transport) during the AD 850–1850. This slow weakening trend is caused by strong, explosive volcanic eruptions during the LIA. After a rapid strengthening in the initial decade after an eruption, the AMOC experiences a slow centennial timescale weakening, driven by radiatively-induced decrease in ocean heat content tied to NADW, which generates sustained surface cooling, reduced surface evaporation, and a consequent increase in the freshwater flux into the subpolar North Atlantic deep convection region. The steady increase in freshwater flux leads to a long-term decline of AMOC. Of particular note in our mechanism is the counterintuitive centennial timescale response to the accumulated impact of short-term volcanic radiative forcing events. However, this response may depend on the mean climate state and model biases[62], introducing uncertainties that warrant further investigation. Despite this, this mechanism has implications for future climate projections. The current AMOC state, for example, is partly determined by the lingering effects of past explosive volcanic forcing events, and the future projected behavior of the AMOC under anthropogenic greenhouse

https://doi.org/10.1038/s41467-026-74873-5

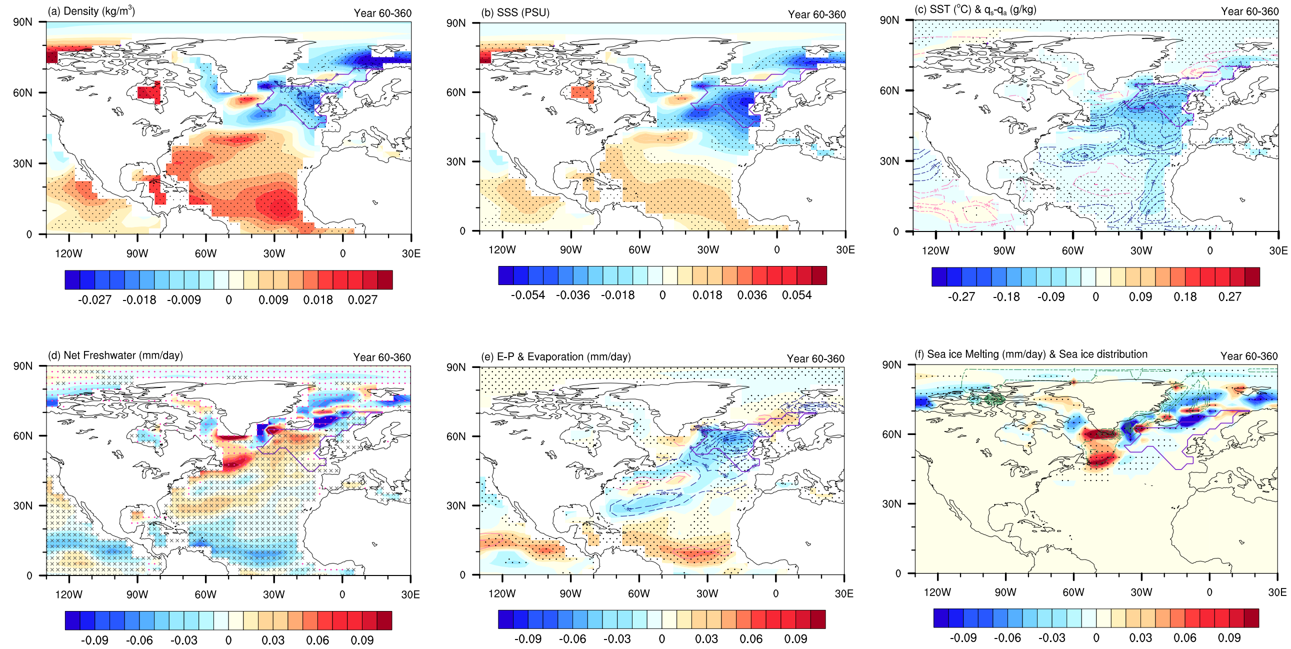

Fig. 4 | Spatial pattern of the density anomaly and freshwater flux during the long-term weak phase of AMOC in the idealized experiments. a–**c** Spatial plot of the ensemble mean neutral potential density (kg/m^3), sea surface salinity (SSS, unit: PSU) and sea surface temperature (unit: °C) overlaied by the difference of saturated specific humidity and air specific humidity (q_s-q_a, unit: g/kg, dahsed contours: blue is negative and red is positive) averaged in years 60–360 of the Samalas-only EXP. **d** Spatial plot of net freshwater flux (mm/day) over the North Atlantic during years 60–360. Pink dots mark the area where NFW is dominated by sea ice melt, and black crosses mark the region where NFW is dominated by E-P. **e** Spatial plot of E-P (unit: mm/day, colored shading), overlaid by evaporation anomalies (dashed contour lines, blue is negative and red is positive, unit: mm/day). **f** Spatial pattern of sea ice melt (unit: mm/day), overlaid by the distribution of sea ice volume (green contour at an interval of 0.4 m^3) in year 60–360. Black dots in (**a**–**c**, **e**, **f**) represent 95% significant interval. The purple lines in each plot show the deep convection area (Fig. S1b). All of the results are applied with 11-year running mean.

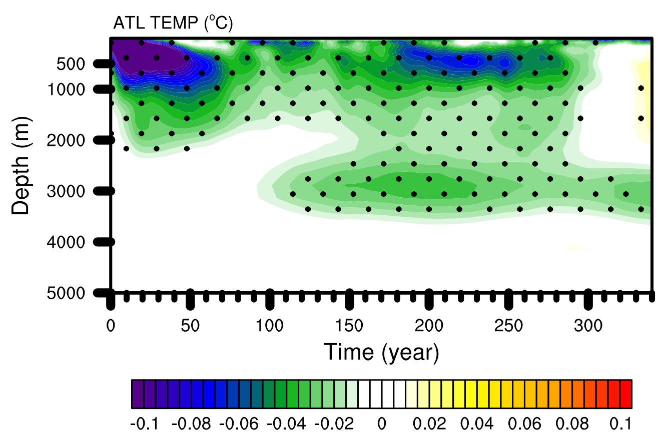

Fig. 5 | Cooling stored in the deep Atlantic Ocean. Hovmöller diagram of the ensemble mean ocean temperature (unit: °C) over the Atlantic (50S–65N, 90W–30E) after volcanic eruptions in the 10 cases of Samalas-only EXP. The X-axis is the time after volcanic eruptions, spanning from year 0 to year 340. The Y-axis is the depth (unit: m) of the ocean. Black dots represent 95% significant interval.

radiative forcing should account for the delayed impact of past radiative volcanic impact on AMOC decades to centuries ago.

Methods

Materials

To our knowledge, there exist eleven paleo AMOC-sensitive indicators. Among these eleven indicators, 5 can be directly related to our model variables and therefore can be assimilated in our models. The other 6 can't be assimilated due to the lack of a forward model relating these AMOC-sensitive indicators to model variables. The first AMOC proxy that can be assimilated is the 100-year smoothed difference of calcite δ^{18}O from benthic foraminifera between Dry Tortugas (540 m) and Great Bahama Bank (530 m) cross the Florida Strait[12]. This AMOC proxy indicates the cross-strait density contrast and, in turn, the strength of the geostrophic flow of the Florida Current (FC), with a larger $\delta^{18}O_c$ contrast corresponding to a stronger FC and therefore AMOC[63]. The second proxy is the difference of $\delta^{18}O_c$ between two planktonic foraminifera species from the south Greenland margin: Neogloboquadrina pachyderma (sinistral coiling) (Nps) at 100–200 m and Turborotalita quinqueloba (Tq) at 25–75 m. This proxy reflects upper ocean thermal stratification, with smaller $\delta^{18}O_{c\text{NPS-Tq}}$ indicating enhanced East Greenland Current (cold and fresh) over the Irminger Current (warm and saline), which in turn suppresses the deep convection in the LS[10,20]. The third proxy is the calcite δ^{18}O retrieved from the Laurentian Channel and is thought to represent the contrast between the cold LS slope water (LSSW) and the warm Atlantic Temperate Slope Water[16]. Since a weaker AMOC is usually consistent with a weaker LS deep convection and less LSSW, the subsurface has a warmer temperature and lower $\delta^{18}O_c$ at this site, which captures the signal of AMOC. The fourth proxy is the difference of subsurface ocean temperature between the North-East SPG and the North-West Atlantic shelf, which is thought to represent the intensity of the deep Labrador Current (LC)[14]. An intensified warm North Atlantic Current and cold LC during the strong phase of AMOC induce a dipole response of warmer NE SPG and colder Gulf Stream extension[14,64]. The last proxy is the warming hole index that is thought to be associated with the AMOC heat transport[6]. This proxy is reconstructed here by averaging the warming hole index provided by Rahmstorf et al.[6] and computed using sea surface temperature (SST) data from the last millennium reanalysis (LMR)[65] prior to 1870, after applying a 51-year smoothing. After 1870, the LMR data is substituted with the average of three observed global SST datasets, including the HadiSST from the Hadley Center[66], the

Kaplan extended SST V2 from the UK Met Office[67], and the NOAA Extended Reconstruction SST[68], because there is a rising trend of the warming hole index in LMR during this period[65]. These five AMOC-sensitive indicators are primarily discussed in the main text.

The six paleo AMOC-sensitive indicators which cannot be assimilated include the percentage of the polar species N. pachyderma (s) (Nps) in the LS, the Sortable silt mean grain size ($\bar{SS}$) from Iceland Basin[10,13] and Cape Hatteras[14], the radiocarbon reservoir age offset ($\triangle R$) from shell chronology in the North Icelandic shelf[11], and the seawater cadmium (Cd) concentrated in the Florida Strait[18]. These proxies exhibit similar declining trends during the LIA (Fig. S11), despite some differences in the timing of the decrease, which could be associated with the chronology uncertainty and coarse temporal resolution, consistent with the five reconstructed AMOC-sensitive indicators introduced above.

The Community Earth System Model Last Millennium Ensemble (CESM-LME) archive is employed to compose synthetic AMOC-sensitive indicators and study the relation between these indicators and AMOC variations in the past millennium. These simulations are driven by the transient forcings spanning from 850 to 2005 CE using CESM1.2[69], with a horizontal resolution of ~1.75° in the ocean component. In particular, the volcanic forcing is that derived from Gao et al.[33] of the past 1500 years. A set of 19 CESM-LME simulations are used, including 1 control experiment (CTRL EXP), 13 all-forcing experiments (ALL EXP), and 5 volcanic-forcing experiments (VOLC EXP). Another set of 3 simulations in the isotope-enabled last millennium ensemble (iLME) from iCESM[70,71] are also used. These iLME simulations use a code similar to that of LME, and has the same resolution, spanning period, and external forcings as in the LME experiments. The climatological AMOC streamfunctions in the preindustrial period are around 24 Sv (for iLME and LME cases). The linear trends of the transport reduction from AD 850 to 1850 range from 0.1 to 0.7 Sv (for iLME and LME cases) with a mean of about 0.4 Sv, representing about 1.6% reduction. Note that the climatological AMOC in iLME2 and iLME3 is underestimated due to a known error in the applied regional masks. The AMOC index for iLME2 and iLME3 simulations is therefore recomputed from the meridional velocity field, while iLME1, which has a reasonable climatology, is used as the representative case in the main analysis.

The meridional overturning circulation is analyzed using two models from the Paleoclimate Modeling Intercomparison Project Phase 3 (PMIP3)/Coupled Model Intercomparison Project Phase 5 (CMIP5), and two models of the PMIP4/CMIP6, for which the AMOC variable is available online in the past millennium experiments. The PMIP3/CMIP5 models include the Max Planck Institute Earth System Model (MPI-ESM-P) and Meteorological Research Institute-Coupled Global Climate Model (MRI-CGCM3), while the PMIP4/CMIP6 models include the Meteorological Research Institute Earth System Model version 2.0 (MRI-ESM2-0), and the Model for Interdisciplinary Research on Climate, Earth Systemversion 2 for Long-term simulations (MIROC-ES2L). The volcanic forcings used in these multi-model simulations are those derived from Geo et al.[33] (MRI-CGCM3), Toohey and Sigl[34] (MRI-ESM2-0 and MIROC-ES2L), and Crowley et al.[35] (MPI-ESM-P).

AMOC index and AMOC-sensitive indicators in the model

In this paper, the AMOC index is defined as the maximum annual mean Atlantic Meridional Overturning Streamfunction between 20°N–50°N and below 500-m, after 11-year running mean.

The definitions of the 5 AMOC-sensitive indicators reproduced in model are consistent with the 5 paleo AMOC-sensitive indicators mentioned above. The first one (Fig. 1h) is defined by the $\delta^{18}O_c$ contrast across the Florida Strait (24.2°N, 85°W minus 24.2°N, 78.5°W, Fig. S1a blue stars) at depth of 530 m[12,63]. The second one (Fig. 1i) is defined by the difference of $\delta^{18}O_c$ at south Greenland margin (58°N, 43°W, Fig. S1a pink circle) in depth of 100–200 and 25–75 m[10,20]. The third one (Fig. 1j) is defined as the $\delta^{18}O_c$ at the entrance of the Laurentia Channel (45°N, 55°W, Fig. S1a yellow triangle) in depth of 350 m. Note that, the reconstruction site (48°N, 68°W) of the AMOC-sensitive indicator in Thibodeau's work[16] is not in the open ocean. Since our model has missing value at that location, we opt for the nearest available site instead. The $\delta^{18}O_c$ used in these 3 indicators is calculated by the sea water oxygen isotope ($\delta^{18}O_w$) and ocean temperature (t in Celsius degree) in the 3 iLME members, following the equation[72]:

$$\delta^{18}O_c = \delta^{18}O_w - 0.27 + 0.0011t^2 - 0.245t + 3.58$$

The fourth indicator (Fig. 1k) is defined as the contrast of upper ocean temperature (100–200 m) over the Northeast NA SPG region (50-62°N, 10-30°W) and Northwest Atlantic shelf (36–46°N, 50–70°W, Fig. S1a green boxes) in the model[14]. The warming hole index (Fig. 1l) is defined as the difference of SST between Subpolar North Atlantic (SPNA, 46–60°N, 15–40°W, Fig. S1a brown box) and North Hemisphere[6]. These three AMOC-sensitive indicators are computed using variables from 3 iLME and 13 LME members.

Paleo data assimilation I: single model PDA in iCESM

We discuss in detail the reconstruction of the AMOC transport index ψ in iCESM. First, the 5 paleo AMOC-sensitive indicators that can be represented in iCESM are interpolated to yearly data; these 5 indicators consist of three involving stable water isotopes (the δ^{18}O difference cross Florida Strait[12], the $\delta^{18}O_{NPS\text{-}Tq}$ at south Greenland margin[10,20], and the δ^{18}O near Laurentia Channel[16]) and two related to ocean temperatures (the dipole pattern of SPG subsurface ocean temperature[14] and the warming hole index[6]) ("Method 1"). These 5 proxies, which are denoted by $\boldsymbol{y}$ (dimension of $p \times 1$, p indicates the number of proxies), are assimilated through an offline PDA[65,73,74] approach. The uncertainty of each proxy, i.e., the observation error variance $\sigma^2_{o,j}$ ($j = 1,\ldots,p$), is here taken, approximately, as its temporal variance. By assuming static and uncorrelated errors, the observation error covariance matrix $\mathbf{R}$ is a diagonal one, with diagonal elements of $\beta\sigma^2_{o,j}$, where $\sigma^2_{o,j}$ is computed as the variance of the proxies after linear detrending and the coefficient $\beta = 0.27$ is determined based on "bootstrapping" DA sensitivity experiments ("Method" below and Fig. S12).

Second, the prior state vector, which contains the model AMOC index to be reconstructed, is obtained. Following Hakim et al.[65], ensemble priors $\boldsymbol{X}^f_{n\times N} = \left\{\boldsymbol{x}^f_1, \ldots, \boldsymbol{x}^f_N\right\}$ where $\boldsymbol{x}$ is the state vector with dimension of $n \times 1$ and N is ensemble size of 100, are randomly drawn from the AMOC index in iLME case 1 (Fig. 1h–m, black dashed line). The 100-member ensemble is used to construct the covariance matrix such that the matrix is not contaminated strongly by sampling errors. By subtracting the prior ensemble mean $\bar{\boldsymbol{x}}^f = \frac{1}{N}\sum_{i=1}^{N}\boldsymbol{x}^f_i$ from each member, the ensemble perturbations $\boldsymbol{x}'^f_i = \boldsymbol{x}^f_i - \bar{\boldsymbol{x}}^f$ $(i = 1, K, N)$ and the square root of sample background error covariance $\boldsymbol{X}'^f = \left[\boldsymbol{x}^f_1 - \bar{\boldsymbol{x}}^f, \boldsymbol{x}^f_2 - \bar{\boldsymbol{x}}^f, K, \boldsymbol{x}^f_N - \bar{\boldsymbol{x}}^f\right]/\sqrt{N-1}$ are obtained. Then, the prior estimate, which is a transformation of the model AMOC index to the observation space of AMOC-sensitive indicators, is calculated. Using the observation forward operator H to transform the state vector to the indicators, the observation priors of ensemble mean $H\left(\bar{\boldsymbol{x}}^f\right)$ (dimension of $p \times 1$) and ensemble priors of observations $H\left(\boldsymbol{x}^f_i\right)$ (dimension of $p \times N$) are achieved, in which each element is estimated model indicator $h_j\left(\bar{\boldsymbol{x}}^f\right)$ and $h_j\left(\boldsymbol{x}^f_i\right)$ (Fig. 1h–l, colored solid lines), respectively. The square root of sample background error covariance in observation space is given by $H\boldsymbol{X}'^f$, in which each element is $\left(h_j(\boldsymbol{x}^f_i) - h_j(\bar{\boldsymbol{x}}^f)\right)/\sqrt{N-1}$.

Third, the prior mean of the AMOC index $\bar{\psi}^f$ from iLME case 1 is updated by assimilating the AMOC-sensitive indicators through an ensemble Kalman filter,

$$\bar{\psi}^a = \bar{\psi}^f + \Psi'^f \left(H\boldsymbol{X}'^f\right)^T \left(H\boldsymbol{X}'^f \left(H\boldsymbol{X}'^f\right)^T + \boldsymbol{R}\right)^{-1} \left[\boldsymbol{y} - H\left(\bar{\boldsymbol{x}}^f\right)\right] \quad (1)$$

where $\Psi'^f = [\psi_1^f - \bar{\psi}^f, \psi_2^f - \bar{\psi}^f, \ldots, \psi_N^f - \bar{\psi}^f]/\sqrt{N-1}$ is a row vector of $\boldsymbol{X}'^f$. The mean analysis increment is proportional to the correlation between the AMOC index and AMOC-sensitive indicators, and also the innovations of observed AMOC-sensitive indicators and estimated ones. The prior perturbations of the AMOC index $\psi_i'^f$ is updated by

$$\psi_i'^a = \psi_i'^f - \Psi'^f (H\mathbf{X}'^f)^T \left[\left(\sqrt{(H\mathbf{X}'^f)(H\mathbf{X}'^f)^T + \boldsymbol{R}}\right)^{-1}\right]^T \left[\sqrt{((H\mathbf{X}'^f)(H\mathbf{X}'^f)^T + \boldsymbol{R})} + \sqrt{\boldsymbol{R}}\right]^{-1} (H\mathbf{X}'^f) \quad (2)$$

From the posterior perturbations of the AMOC index, the uncertainty of the posterior mean $\bar{\psi}^a$, i.e., the analysis variance σ_a^2, can be computed.

To estimate the optimal observational error covariance, a bootstrap-based sensitivity approach is used. The optimal observational error is determined by optimizing the coefficient β. Five "bootstrapping" sensitivity experiments are performed to obtain the optimal coefficient β for the observational error covariance R, while similar strategies to "bootstrapping" have been used to adaptively estimate data assimilation parameters (e.g., localization length scale)[74,75]. In each sensitivity test, 4 of the 5 paleo AMOC-sensitive indicators are used for assimilation with coefficient β ranging from 0.1 to 1 (Fig. S12), and the DA results (Fig. S12, colored solid lines) are compared with the fifth indicator that was not used in the assimilation (Fig. S12, black dashed line). Two methods are used to assess the sensitivity of DA AMOC to the optimal coefficient β.

Firstly, the root mean square error (RMSE) of each DA AMOC-sensitive indicator (normalized and applied with 100 years running mean) and paleo AMOC-sensitive indicator (normalized) left out of the assimilation is calculated. RMSE reaches the minimum for $\beta = 0.1$, 0.2, 0.2, 0.1, and 0.6 in each of the 5-sensitivity test, respectively. The equal weight average of the error covariance gives the optimal $\beta = (0.1 + 0.2 + 0.2 + 0.1 + 0.6)/5 = 0.24$.

Secondly, DA AMOC transport is compared with the paleo AMOC transport. In our study, DA AMOC transport is defined as: $\mathrm{Trend}_{\mathrm{DA}} \times$ year, where $\mathrm{Trend}_{\mathrm{DA}}$ is the trend of DA AMOC, and year is the length of the DA AMOC. Paleo AMOC transport is obtained by the equation: $(\mathrm{Trend}_{\mathrm{paleo}}/\mathrm{Cli}_{\mathrm{paleo}}) \times \mathrm{AMOC}_{\mathrm{model}} \times$ year, in which $\mathrm{Trend}_{\mathrm{paleo}}$ is the trend of the paleo AMOC-sensitive indicators not involved in the assimilation, $\mathrm{Cli}_{\mathrm{paleo}}$ indicates the climatology of the paleo AMOC-sensitive indicators, and $\mathrm{AMOC}_{\mathrm{model}}$ represents the climatology of the model AMOC index, which is 24 Sv in our case. The DA and paleo AMOC transport are most similar when β equals to 0.1, 0.1, 0.5, 0.1, and 0.7 for each sensitivity test, respectively. The equal weight average of the error covariance coefficient is therefore $\beta = (0.1 + 0.1 + 0.5 + 0.1 + 0.7)/5 = 0.3$.

As the β value evaluated in these two methods are similar, we finally use $\beta = (0.24 + 0.3)/2 = 0.27$ for the optimal error covariance for assimilation.

A perfect model test is conducted to validate our PDA method. Firstly, data assimilation is performed with the five model AMOC-sensitive indicators from iLME1 being treated as observations, and the model AMOC index simulated in iLME3 as prior. It shows that the assimilated AMOC (Fig. S13a, red line) is highly correlated with the true AMOC index simulated in iLME1 (Fig. S13a, black solid line), despite the prior AMOC index from iLME3 (Fig. S13a, black dashed line) differing from the true AMOC. This highlights the effect of covariance in assimilating. Similar results can also be found when using iLME case3 as observation and iLME case 1 as prior (Fig. S13b), as well as in the cross-validations between iLME1 and iLME2, and between iLME2 and iLME3 (Fig. S13c–f). These findings confirm the reliability of the PDA method.

Paleo data assimilation II: multi-model PDA using PMIP simulations

The iCESM is used for off-line PDA first because it can assimilate most of the AMOC-sensitive indicators, especially the three indicators related to δ^{18}O. But using a single model leaves the model uncertainty unaccounted for. Ideally, model uncertainty can be accounted for by using multiple models, such as the other 4 PMIP models (Materials). These PIMP models, however, do not incorporate water isotopes and therefore can only assimilate two temperature-related proxies: the dipole pattern of SPG subsurface ocean temperature[14] and the warming hole index (Materials)[6]. To account for the model uncertainty in PDA, we therefore take the following approach.

First, we tested in iCESM that the AMOC declining trend is similar by assimilating all the 5 proxies or only the 2 temperature-related ones. Specifically, in the CESM-iLME simulation (case 1), we use the same off-line PDA approach described above but assimilate only the two temperature proxies in observations. The optimal error coefficient is found to be about $\beta = 0.2$ and the assimilated AMOC exhibits a declining trend of about 0.7 ± 0.3 Sv in AD 850–1850 (Fig. S4a). This trend is similar to that when all the 5 proxies are assimilated as discussed above.

Based on the iCESM test above, we assume that the assimilation of the two temperature proxies alone is sufficient for the AMOC assimilation in the four PMIP model simulations. We then apply the same off-line PDA approach discussed above in the four PMIP models, but only using the two temperature proxies. Now, the optimal observational error coefficient in each model is tested with two "bootstrapping" sensitivity experiments, with 1 of the 2 proxies being used for assimilation and the other for comparison. The optimum error covariance selected for each model is 0.3 R (MPI-ESM-P), 0.7 R (MRI-CGCM3), 0.65 R (MRI-ESM2-0), 0.33 R (MIROC-ES2L). All four assimilated AMOCs show a declining trend in AD 850–1850, with a magnitude of −0.5 ± 0.3 Sv (MPI-ESM-P), −0.5 ± 0.3 Sv (MRI-CGCM3), −0.5 ± 0.4 Sv (MRI-ESM2-0), and −0.6 ± 0.3 Sv (MIROC-ES2L) (Fig. S4b–e). As in iCESM, these PDA AMOC declining trends are all greater than those in each model itself, because the AMOC-sensitive indicators exhibit a greater trend in the observation than in the model. Combining the assimilated AMOCs in the 4 PMIP models with that in iCESM, we give our best estimation of the AMOC declining as the cross-model ensemble mean as (−1.2-0.5-0.5-0.5-0.6)/5 = −0.7 Sv, with the cross-model ensemble spread as 0.27 Sv. In each individual model, the analysis uncertainty is about $(0.30 + 0.3 + 0.3 + 0.4 + 0.3)/5 = 0.32$ Sv. Therefore, the total uncertainty for the AMOC transport with multi-model assimilation is taken approximately as the square root of both as $\sqrt{0.27^2 + 0.32^2} = 0.4$ Sv. This gives our multi-model PDA AMOC declining trend of the pre-industrial last millennium as $-0.7 \pm 0.4Sv$. We note that this uncertainty is applied to the trend of DA AMOC in AD 850–1850, but not the uncertainty at any instant. Therefore, the uncertainty would be much greater than $\pm 0.4Sv$ at any given time due to the large uncertainty in the proxy data and models.

Model description and sensitivity experimental design

In this paper, the Community Earth System Model Version 1.2 (CESM1.2) is used for the idealized volcanic sensitivity experiment. CESM is an outstanding model that can effectively capture climate changes in the past millennium as well as characteristics of AMOC[36,37]. It has a horizontal resolution of ~3.75° in the atmosphere and land component, ~2.5° in the ocean component, and 60 vertical levels in the ocean. We first run a 1300-year spinning-up experiment based on the initial climate condition of AD1850 and then a 600-year CTRL experiment. In our experiment, the reconstructed sulfate aerosol of MT.

Samalas (257.91 Tg) in AD 1258 (referred to as AD 1257 in some other papers[76] is derived from IVI2[33]. The only forcing used in the sensitivity experiment (Samalas EXP) is the injection of volcanic aerosol into the stratosphere of the atmosphere in April of a year of strong AMOC state from the CTRL. This eruption, which is the largest volcanic event in the past 2000 years, is located in the tropical region of Indonesia peninsula. Its sulfate aerosols, persisting for 5 years in the stratosphere (above 100 hPa), are mainly concentrated between 30°S to 30°N and decaying poleward with a near-symmetric distribution across hemispheres[33]. A total of 10 members are integrated, each for 360 years, by injecting volcanic forcing at the same year of CTRL, with small disturbances (order 10^{-14} °C) added to the initial atmospheric temperature field. Additionally, to evaluate the impacts of varying AMOC initial states, two supplementary sets of experiments are conducted by imposing the same Samalas volcanic forcings at a neutral and a weak AMOC state in the CTRL, each comprising 3 ensemble members and integrated over 360 years. Monthly output data is analyzed. The major result of the experiment here is the different AMOC response between the initial and later stages, with the initial and later stages characterized, respectively, by a strong intensification in the initial decade followed by a slow weakening of centinneil time scale. This feature is insensitive to different initial AMOC states (Fig. S5), and is further shown robust in PMIP simulations (Fig. S4).

The deep convection region

The deep convection region studied in this paper is defined as the region where winter (DJFMA) maximum mixed layer depth in subpolar NA (north of 45°N) is greater than 150 m (Fig. S1b), including the Irminger Sea, Iceland Basin, Iceland-Faroe-Scotland Ridge, as well as Norwegian Sea. Note that model biases in simulating deep convection regions, such as its underestimation in the LS or Nordic Seas, are common limitations in paleoclimate simulations[77]. While this may affect regional oceanic processes[78,79], it does not fundamentally alter the large-scale AMOC variability discussed in this study[4,37]. Further improvements in representing deep convection and associated deep-ocean dynamical processes are needed for future studies.

Data availability

The simulations from the Community Earth System Model (CESM) Last Millennium Ensemble (LME) Project are freely available through Otto-Bliesner et al.[69] and NCAR, and supercomputing resources are provided by NSF/CISL/Yellowstone. The Last Millennium Ensemble simulations derived from isotope-enabled model is available through Brady et al.[70] and Stevensen et al.[71]. The Last Millennium Reanalysis (LMR) data used in the manuscript are freely available in Hakim et al.[65]. The reconstructed Ice-core-based global volcanic aerosol from Gao et al.[33] is released at http://climate.envsci.rutgers.edu/IVI2/, from Toohey and Sigl[34] is released at https://www.wdc-climate.de/ui/entry?acronym=eVolv2k_v3, and from Crowley et al.[35] is released at https://www.ncei.noaa.gov/access/paleo-search/study/14168. The eleven paleo AMOC proxies analyzed in this paper are taken from Lund et al.[12], Moffa-Sánchez et al.[10,20], Thibodeau et al.[16], Thornalley et al.[14], Rahmstorf et al.[6], Wanamaker et al.[11], Mjell et al.[13], Valley et al.[18]. The observed ERSST[68] is released at https://www.ncei.noaa.gov/products/extended-reconstructed-sst, the HadiSST[66] is released at http://www.metoffice.gov.uk/hadobs/hadisst, and the Kaplan extended SST[67] is released at https://www.psl.noaa.gov/data/gridded/data.kaplan_sst.html. The paleo-data assimilated AMOC and Samalas volcanic sensitivity experimental data generated in this study are deposited in the Figshare repository at: https://doi.org/10.6084/m9.figshare.28324124.

References

1. Liu, Z. Evolution of Atlantic Meridional Overturning Circulation since the Last glaciation: model simulations and relevance to present and future. *Philos. Trans. A* **381**, 20220190 (2023).
2. Zhang, R. et al. A review of the role of the Atlantic Meridional Overturning Circulation in Atlantic multidecadal variability and associated climate impacts. *Rev. Geophys.* **57**, 316–375 (2019).
3. Zhang, X., Knorr, G., Lohmann, G. & Barker, S. Abrupt North Atlantic circulation changes in response to gradual CO_2 forcing in a glacial climate state. *Nat. Geosci.* **10**, 518–523 (2017).
4. Yin, Q. Z., Wu, Z., Berger, P. A. & Goosse, H. Insolation triggered abrupt weakening of Atlantic circulation at the end of interglacials. *Science* **373**, 1035–1040 (2021).
5. Bryden, H. L., Hannah, R., Longworth, C. & Stuart, A. Slowing of the Atlantic Meridional Overturning Circulation at 25° N. *Nature* **438**, 655–657 (2005).
6. Rahmstorf, S. Exceptional twentieth-century slowdown in Atlantic Ocean overturning circulation. *Nat. Clim. Change* **5**, 475–480 (2015).
7. Zhu, C., Liu, Z., Zhang, S. & Wu, L. Likely accelerated weakening of Atlantic overturning circulation emerges in optimal salinity fingerprint. *Nat. Commun.* **14**, 1245 (2023).
8. IPCC. *Contribution of Working Groups I, II and III to the Sixth Assessment Report of the Intergovernmental Panel on Climate Change* (eds Lee, H. & Romero, J.), Climate Change 2023: Synthesis Report (IPCC, 2023).
9. Ditlevsen, P. & Ditlevsen, S. Warning of a forthcoming collapse of the Atlantic Meridional Overturning Circulation. *Nat. Commun.* **14**, 4254 (2023).
10. Moffa-Sánchez, P. & Hall, I. R. North Atlantic variability and its links to European climate over the last 3000 years. *Nat. Commun.* **8**, 1726 (2017).
11. Wanamaker, A. D., Butler, P. G. & Scourse, J. D. Surface changes in the North Atlantic meridional overturning circulation during the last millennium. *Nat. Commun.* **3**, 899 (2012).
12. Lund, D. C., Lynch-Stieglitz, J. & Curry, W. B. Gulf stream density structure and transport during the last millennium. *Nature* **444**, 601–604 (2005).
13. Mjell, T. L., Ninnemann, U. S., Kleiven, H. elgaF. & Hall, I. R. Multidecadal changes in Iceland Scotland overflow water vigor over the last 600 years and its relationship to climate. *Geophys. Res. Lett.* **43**, 5 (2016).
14. Thornalley, D. J. R. et al. Anomalously weak Labrador Sea convection and Atlantic overturning during the past 150 years. *Nature* **556**, 227–230 (2018).
15. Caesar, L., McCarthy, G. D., Thornalley, D. J. R., Cahill, N. & Rahmstorf, S. Current Atlantic Meridional Overturning Circulation weakest in last millennium. *Nat. Geosci.* **14**, 118–120 (2021).
16. Thibodeau, B., Not, C. & Zhu, J. Last century warming over the Canadian Atlantic shelves linked to weak Atlantic Meridional Overturning Circulation. *Geophys. Res. Lett.* **45**, 12, 376–312, 385 (2018).
17. Moffa-Sánchez, P. et al. Variability in the northern North Atlantic and Arctic oceans across the last two millennia: a review. *Paleoceanogr. Paleoclimatol.* **34**, 1399–1436 (2019).
18. Valley, S. G., Lynch-Stieglitz, J., Marchitto, T. M. & Oppo, D. W. Seawater cadmium in the Florida Straits over the Holocene and implications for upper AMOC variability. *Paleoceanogr. Paleoclimatol.* **37**, e2021PA004379 (2022).
19. Drijfhout, S., Gleeson, E., Dijkstra, H. A. & Livina, V. Spontaneous abrupt climate change due to an atmospheric blocking-sea-ice-ocean feedback in an unforced climate model simulation. *Proc. Natl. Acad. Sci. USA* **110**, 19713–19718 (2013).
20. Moffa-Sanchez, P., Born, A., Hall, I. R., Thornalley, D. J. R. & Barker, S. Solar forcing of North Atlantic surface temperature and salinity over the past millennium. *Nat. Geosci.* **7**, 275–278 (2014).
21. Lapointe, F. & Bradley, R. S. Little Ice Age abruptly triggered by intrusion of Atlantic waters into the Nordic Seas. *Sci. Adv.* **7**, eabi8230 (2021).

22. Schleussner, C. F. & Feulner, G. Was the Little Ice Age the result of a volcanically-triggered regime shift in the North Atlantic Ocean circulation? *Climate* **9**, 1321–1330 (2013).
23. Mann, M. E., Steinman, B. A., Brouillette, D. J. & Miller, S. onyaK. Multidecadal climate oscillations during the past millennium driven by volcanic forcing. *Science* **371**, 1014–1019 (2021).
24. Mann, M. E., Steinman, B. A. & Miller, S. K. Absence of internal multidecadal and interdecadal oscillations in climate model simulations. *Nat. Commun.* **11**, 49 (2020).
25. Zhong, Y., Miller, G. H. & Ottobliesner, B. L. Arctic climate response to decadally-paced explosive volcanism in CCSM3. *Clim. Dyn.* **37**, 2373–2387 (2010).
26. Pausata, F. S. R., Chafik, L. & Caballero, R. Impacts of high-latitude volcanic eruptions on ENSO and AMOC. *Proc. Natl. Acad. Sci. USA* **112**, 13784 (2015).
27. Slawinska, J. & Robock, A. Impact of volcanic eruptions on decadal to centennial fluctuations of Arctic Sea ice extent during the last millennium and on initiation of the Little Ice Age. *J. Clim.* **31**, 2145–2167 (2018).
28. Stenchikov, G., Delworth, T. L. & Ramaswamy, V. Volcanic signals in oceans. *J. Geophys. Res. Atmos.* **114**, D16 https://doi.org/10.1029/2008JD011673 (2009).
29. Ortega, P., Marisa, M., Fidel, G., R., Juliette, M. & Legutke, S. Variability of the Atlantic Meridional Overturning Circulation in the last millennium and two IPCC scenarios. *Clim. Dyn.* **38**, 1925–1947 (2012).
30. Ottera, O. H., Bentsen, M., Drange, H. & Suo, L. External forcing as a metronome for Atlantic multidecadal variability. *Nat. Geosci.* **3**, 688–694 (2010).
31. Mignot, J., Khodri, M. & Frankignoul, C. Volcanic impact on the Atlantic Ocean over the last millennium. *Clim. Past Discuss.* **7**, 1439–1455 (2011).
32. Zanchettin, D., Timmreck, C. & Graf, H. F. Bi-decadal variability excited in the coupled ocean-atmosphere system by strong tropical volcanic eruptions. *Clim. Dyn.* **39**, 419–444 (2012).
33. Gao, C., Robock, A. & Ammann, C. Volcanic forcing of climate over the past 1500 years: an improved ice. *J. Geophys. Res. Oceans* **113** https://doi.org/10.1029/2008JD010239 (2008).
34. Toohey, M. & Sigl, M. Volcanic stratospheric sulphur injections and aerosol optical depth from 500 BCE to 1900 CE. *Earth Syst. Sci. Data Discuss.* **9**, 809–831 (2017).
35. Crowley, T. J. & Unterman, M. B. Technical details concerning development of a 1200-yr proxy index for global volcanism. *Earth Syst. Sci. Data Discuss.* **5**, 187–197 (2012).
36. Hu, A., Meehl, G. & Rosenbloom, N. The influence of variability in meridional overturning on global ocean circulation. *J. Clim.* **34**, 7697–7716 (2021).
37. Yang, H., Jiang, R. & Wen, Q. The role of mountains in shaping the global meridional overturning circulation. *Nat. Commun.* **15**, 2602 (2024).
38. Moat, B. I. et al. Atlantic meridional overturning circulation observed by the RAPID-MOCHA-WBTS (RAPID-Meridional Overturning Circulation and Heatflux Array-Western Boundary Time Series) array at 26N from 2004 to 2022 (v2022.1), (British Oceanographic Data Centre - Natural Environment Research Council, 2023).
39. Menary, M. B. et al. Aerosol-forced AMOC changes in CMIP6 historical simulations. *Geophys. Res. Lett.* **47**, e2020GL088166 (2020).
40. Swingedouw, D. et al. Bidecadal North Atlantic Ocean circulation variability controlled by timing of volcanic eruptions. *Nat. Commun.* **6**, 6545 (2015).
41. Wang, T., Otterå, O. H. & Gao, Y. The response of the North Pacific decadal variability to strong tropical volcanic eruptions. *Clim. Dyn.* **39**, 2917–2936 (2012).
42. Zanchettin, D. Delayed winter warming: a robust decadal response to strong tropical volcanic eruptions? *Geophys. Res. Lett.* **40**, 204–209 (2012).
43. Sjolte, J., Sturm, C. & Adolphi, F. Solar and volcanic forcing of North Atlantic climate inferred from a process-based reconstruction. *Climate* **14**, 1179–1194 (2018).
44. Hernández, A. et al. Modes of climate variability: synthesis and review of proxy-based reconstructions through the Holocene. *Earth Sci. Rev.* **209**, 103286 (2020).
45. Arellano-Nava, B. et al. Destabilisation of the subpolar North Atlantic prior to the Little Ice Age. *Nat. Commun.* **13**, 5008 (2022).
46. Miles, M. W., Andresen, C. S. & Dylmer, C. V. Evidence for extreme export of Arctic sea ice leading the abrupt onset of the Little Ice Age. *Sci. Adv.* **6**, eaba4320 (2020).
47. Liu, Z. et al. Strong red noise ocean forcing on Atlantic multidecadal variability assessed from surface heat flux: theory and application. *J. Clim.* **36**, 55–80 (2022).
48. Gulev, S. et al. North Atlantic Ocean control on surface heat flux on multidecadal timescales. *Nature* **499**, 464–467 (2013).
49. Zhang, R. On the persistence and coherence of subpolar sea surface temperature and salinity anomalies associated with the Atlantic multidecadal variability: persistence and coherence of SST and SSS. *Geophys. Res. Lett.* **44**, 7865–7875 (2017).
50. Gu, P., Liu, Z. & Delworth, T. L. Strong oceanic forcing on decadal surface temperature variability over global ocean. *Geophys. Res. Lett.* **51**, e2023GL107401 (2024).
51. Gebbie, G. & Huybers, P. The Little Ice Age and 20th-century deep Pacific cooling. *Science* **363**, 70–74 (2019).
52. Gupta, M. & Marshall, J. The climate response to multiple volcanic eruptions mediated by ocean heat uptake: damping processes and accumulation potential. *J. Clim.* **31**, 8669–8687 (2018).
53. Bagnell, A. T. D. 20th century cooling of the deep ocean contributed to delayed acceleration of Earth's energy imbalance. *Nat. Commun.* **12**, 4604 (2021).
54. Keigwin, L. D. et al. The 8200 year B.P. event in the slope water system, western subpolar North Atlantic. *Paleoceanography* **20**, PA2003 (2005).
55. Sachs, J. ulianP. Cooling of Northwest Atlantic slope waters during the Holocene. *Geophys. Res. Lett.* **34**, 340–354 (2007).
56. Bendle, J. A. P. & Rosell-Mele, A. High-resolution alkenone sea surface temperature variability on the North Icelandic Shelf: implications for Nordic Seas palaeoclimatic development during the Holocene. *Holocene* **17**, 9–24 (2007).
57. Thornalley, D., Elderfield, H. & McCave, I. Holocene oscillations in temperature and salinity of the surface subpolar North Atlantic. *Nature* **457**, 711–714 (2009).
58. Morley A. et al. Solar modulation of North Atlantic Central water formation at multidecadal timescales during the late Holocene. *Earth Planet. Sci. Lett.* **308**, 161–171 (2011).
59. Alonso-Garcia, M. et al. Freshening of the Labrador Sea as a trigger for Little Ice Age development. *Climate* **13**, 317–331 (2017).
60. Zhong, Y. et al. Asymmetric cooling of the Atlantic and Pacific Arctic during the past two millennia: a dual observation-modeling study. *Geophys. Res. Lett.* **45**, 12–497 (2018).
61. Lehner, F. et al. Amplified inception of European Little Ice Age by sea ice-ocean–atmosphere feedbacks. *J. Clim.* **26**, 7586–7602 (2013).
62. Dutta, D. et al. State-dependent North Atlantic response to volcanic eruption clusters. *Geophys. Res. Lett.* **52**, e2025GL117582 (2025).
63. Gu, S., Liu, Z. & Lynch, J. Assessing the ability of zonal à18O contrast in benthic foraminifera to reconstruct deglacial evolution of Atlantic Meridional Overturning Circulation. *Paleoceanogr. Paleoclimatol.* **34**, 800–812 (2019).

64. Zhang, R. Coherent surface-subsurface fingerprint of the Atlantic Meridional Overturning Circulation. *Geophys. Res. Lett.* **35**, L20705 (2008).
65. Hakim, G. J. et al. The last millennium climate reanalysis project: framework and first results. *J. Geophys. Res. Atmos.* **121**, 6745–6764 (2016).
66. Rayner, N. A. et al. Global analyses of sea surface temperature, sea ice, and night marine air temperature since the late nineteenth century. *J. Geophys. Res.* **108**, 4407 (2003).
67. Kaplan, A. et al. Analyses of global sea surface temperature 1856-1991. *J. Geophys. Res. Atmos.* **103**, 18, 567–518, 589 (1998).
68. Huang, B. et al. Extended reconstructed sea surface temperature version 4 (ERSST.v4). Part I: upgrades and intercomparisons. *J. Clim.* **28**, 911–930 (2015).
69. Otto-Bliesner, B. L. et al. Climate variability and change since 850 C.E.: an ensemble approach with the community earth system model (CESM). *Bull. Am. Meteorol. Soc.* **97**, 735–754 (2017).
70. Brady, E. et al. The connected isotopic water cycle in the Community Earth System Model version 1. *J. Adv. Model. Earth Syst.* **11**, 2547–2566 (2019).
71. Stevenson, S. et al. Volcanic eruption signatures in the isotope-enabled last millennium ensemble. *Paleoceanogr. Paleoclimatol.* **34**, 1534–1552 (2019).
72. Marchitto, T. M. et al. Improved oxygen isotope temperature alibrations for cosmopolitan benthic foraminifera. *Geochim. Cosmochim. Acta* **130**, 1–11 (2014).
73. Tardif, R., Hakim, G. J. & Perkins, W. A. Last millennium reanalysis with an expanded proxy database and seasonal proxy modeling. *Climate* **15**, 1251–1273 (2019).
74. Lei, L. & Anderson, J. L. Comparisons of empirical localization techniques for ensemble Kalman filters in a simple atmospheric general circulation model. *Mon. Weather Rev.* **142**, 739–754 (2014).
75. Tierney, J. E., Zhu, J. & King, J. Glacial cooling and climate sensitivity revisited. *Nature* **584**, 569–573 (2020).
76. Lavigne, F. et al. Source of the great A.D. 1257 mystery eruption unveiled, Samalas volcano, Rinjani volcanic complex, Indonesia. *Proc. Natl. Acad. Sci. USA* **110**, 16742–16747 (2013).
77. Roberts, M. J. et al. Sensitivity of the Atlantic Meridional Overturning Circulation to model resolution in CMIP6 HighResMIP simulations and implications for future changes. *J. Adv. Model. Earth Syst.* **12**, e2019MS002014 (2020).
78. Rhein, M. et al. Deep water formation, the subpolar gyre, and the meridional overturning circulation in the subpolar North Atlantic. *Deep Sea Res. Part II Top. Stud. Oceanogr.* **58**, 1819–1832 (2011).
79. de Boyer-Montégut, C. Mixed layer depth climatology computed with a density threshold criterion of 0.03 kg m^{-3} from 10 m depth. *SEANOE*. https://doi.org/10.17882/91774 (2023).

Acknowledgements
The CESM-LME data were generated by the CESM Paleoclimate Working Group at NCAR and the CESM1(CAM5) Last Millennium Ensemble Community Project. The ERSST is provided by the National Oceanic and Atmospheric Administration (NOAA), the HadiSST is provided by the Hadley Center, and the Kaplan extended SST is released by the UK Met Office. This research was jointly supported by the National Key Research and Development Program of China (Grant No. 2023YFF0804700), the US National Science Foundation (Grant No. AGS-2303577), the Science and Technology Innovation Project of Laoshan Laboratory (Grant No. LSKJ202203300), and the National Natural Science Foundation of China (Grant Nos. 42130604, 42575050, 42475051, 42575051, 42111530182, and 42075049).

Author contributions
Conceptualization: L. Ning, Z. Liu, and K. Chen. Methodology: K. Chen, Z. Liu, L. Ning, L. Lei, Michael E. Mann, H. Sun, W. Sun, and W. Hu. Investigation: K. Chen, Z. Liu, and L. Ning. Visualization: K. Chen. Funding acquisition: Z. Liu, L. Ning. Project administration: Z. Liu, L. Ning. Supervision: Z. Liu, L. Ning. Writing-original draft: K. Chen, Z. Liu, and L. Ning. Writing-review & editing: K. Chen, Z. Liu, L. Ning, L. Lei, Michael E. Mann, J. Liu, M. Yan, W. Sun, H. Sun, W. Hu, P. Gu, Y. Bao, L. Li, J. Du, Y. Qin, F. Xing, and W. Qin.

Competing interests
The authors declare no competing interests.

Additional information
Supplementary information The online version contains Supplementary material available at https://doi.org/10.1038/s41467-026-74873-5.

Correspondence and requests for materials should be addressed to Zhengyu Liu or Liang Ning.

Peer review information *Nature Communications* thanks Simon Michel and the other anonymous reviewer(s) for their contribution to the peer review of this work. A peer review file is available.

Reprints and permissions information is available at http://www.nature.com/reprints

Publisher's note Springer Nature remains neutral with regard to jurisdictional claims in published maps and institutional affiliations.